LETTER

https://doi.org/10.1038/s41586-019-1397-7

Rotation tracking of genome-processing enzymes using DNA origami rotors

Pallav Kosuri[1,2,3,7], Benjamin D. Altheimer[1,2,3,4,7], Mingjie Dai[4,5,6], Peng Yin[5,6] & Xiaowei Zhuang[1,2,3]*

Many genome-processing reactions, including transcription, replication and repair, generate DNA rotation. Methods that directly measure DNA rotation, such as rotor bead tracking[1–3], angular optical trapping[4] and magnetic tweezers[5], have helped to unravel the action mechanisms of a range of genome-processing enzymes that includes RNA polymerase (RNAP)[6], gyrase[2], a viral DNA packaging motor[7] and DNA recombination enzymes[8]. Despite the potential of rotation measurements to transform our understanding of genome-processing reactions, measuring DNA rotation remains a difficult task. The time resolution of existing methods is insufficient for tracking the rotation induced by many enzymes under physiological conditions, and the measurement throughput is typically low. Here we introduce origami-rotor-based imaging and tracking (ORBIT), a method that uses fluorescently labelled DNA origami rotors to track DNA rotation at the single-molecule level with a time resolution of milliseconds. We used ORBIT to track the DNA rotations that result from unwinding by the RecBCD complex, a helicase that is involved in DNA repair[9], as well as from transcription by RNAP. We characterized a series of events that occur during RecBCD-induced DNA unwinding—including initiation, processive translocation, pausing and backtracking—and revealed an initiation mechanism that involves reversible ATP-independent DNA unwinding and engagement of the RecB motor. During transcription by RNAP, we directly observed rotational steps that correspond to the unwinding of single base pairs. We envisage that ORBIT will enable studies of a wide range of interactions between proteins and DNA.

To enable the high-resolution tracking of enzyme-induced DNA rotation at the single-molecule level, we used DNA origami—a technology that enables the design and assembly of custom three-dimensional nanostructures with high precision, yield and reproducibility[10,11]—to design an amplifying rotor with fast response times (Fig. 1a, Extended Data Fig. 1a–d, Supplementary Table 1). Our rotor comprises four blades, each of which extends 80 nm perpendicular to the axis of rotation. A double-stranded DNA (dsDNA) segment emerges from the centre of the rotor along the axis of rotation; this segment serves as the substrate for DNA-interacting enzymes (Fig. 1a). We designed the rotor blades to be sufficiently long to not only substantially amplify the motion of the DNA but to also have low hydrodynamic drag and high torsional stiffness (to minimize the obscuring effect of Brownian fluctuations), thereby enabling measurements at a high spatiotemporal resolution (Supplementary Discussion). To enable image-based tracking, we labelled the tip of one of the rotor blades with fluorescent dyes. Atomic force microscopy showed that rotor assembly was successful, with high yield (Fig. 1b, Extended Data Fig. 1e).

We characterized the mechanical properties of the origami rotor–dsDNA complexes by anchoring them to a coverglass surface via an origami tripod (Extended Data Fig. 1f–i, Supplementary Tables 2, 3) and measuring the rotational Brownian motion of the rotor. The power spectrum of the rotor movements revealed a Lorentzian frequency response that is typical of Brownian dynamics in a harmonic potential well (Extended Data Fig. 2a). From these spectra, we obtained the torsional stiffness (κ) and relaxation time constant (τ) of the rotor complexes as a function of the length of the dsDNA segment, as well as the hydrodynamic drag (γ) of the complexes as a function of solution viscosity (Extended Data Fig. 2b–d, Supplementary Discussion). The dependence of κ on the length of the dsDNA segment yielded an apparent torsional-rigidity constant (C) for the DNA of $C = 200 \pm 10$ pN nm^2 rad^{-1} (Supplementary Discussion), which is consistent with previously measured values under no applied stretching force[12]. Using the κ and γ parameters, we estimated the angular fluctuation due to Brownian motion as a function of integration time for a DNA rotor connected to a 52-base-pair (bp) dsDNA segment, and found quantitative agreement with the experimentally measured angular uncertainty (Extended Data Fig. 2e, Supplementary Discussion). Our results showed that only 20 ms were required to resolve single base-pair rotation (34.6°) with a signal-to-noise ratio of 3 (Extended Data Fig. 2e). By comparison, other torque-free methods for tracking DNA rotation require integration times of between 80 ms and more than an hour to achieve the same angular precision, and also require the application of a stretching force[3,8].

To demonstrate the capabilities of ORBIT, we used this method to study the RecBCD helicase, which detects double-stranded breaks and initiates homologous recombination[9]. As RecBCD unwinds dsDNA, its two motors (RecB and RecD) each track along one DNA strand[9]; this is expected to generate a rotation of the DNA with respect to the enzyme of about 34.6° per unwound base pair. However, the rapid unwinding rate of the enzyme[13–17] has thus far precluded observation of DNA rotation induced by RecBCD. To directly measure this rotation, we adsorbed RecBCD onto the surface of a microscope coverglass, and used a flow system to introduce dsDNA substrates, each 80 bp in length and attached to an origami rotor (Fig. 1a). In the presence of ATP, the DNA rotation generated by the unwinding induced by RecBCD should be amplified by the rotor, and cause processive motion of the fluorescent dyes along a circular path. Using a total internal reflection fluorescence microscope, we tracked the dyes with a precision of about 10–15 nm and sampling rates up to 1 kHz (Extended Data Fig. 2f).

We imaged hundreds of single-molecule trajectories in parallel per experiment, and many single-molecule ORBIT trajectories showed unidirectional movements of the fluorescent dyes along a circle with a diameter that was approximately equal to the diameter of the rotor (Fig. 1c, Supplementary Video 1, Supplementary Methods). We converted the angular measurement into the position of RecBCD along the dsDNA by using the average DNA twist of 34.6° per base pair, and determined the unwinding rate under a range of concentrations of ATP (Fig. 1d, e). Although the unwinding rates of individual RecBCD molecules at each ATP concentration exhibited a broad distribution (Extended Data Fig. 3) (consistent with previous studies[14,16,17]), the unwinding rate averaged over the ensemble showed a clear Michaelis–Menten ATP dependence with a Michaelis constant (K_M) of 124 ± 12 μM and a maximum rate (v_{max}) of 304 ± 13 bp s^{-1}, which

[1]Howard Hughes Medical Institute, Harvard University, Cambridge, MA, USA. [2]Department of Chemistry and Chemical Biology, Harvard University, Cambridge, MA, USA. [3]Department of Physics, Harvard University, Cambridge, MA, USA. [4]Graduate Program in Biophysics, Harvard University, Cambridge, MA, USA. [5]Wyss Institute for Biologically Inspired Engineering, Harvard Medical School, Boston, MA, USA. [6]Department of Systems Biology, Harvard Medical School, Boston, MA, USA. [7]These authors contributed equally: Pallav Kosuri, Benjamin D. Altheimer. *e-mail: zhuang@chemistry.harvard.edu

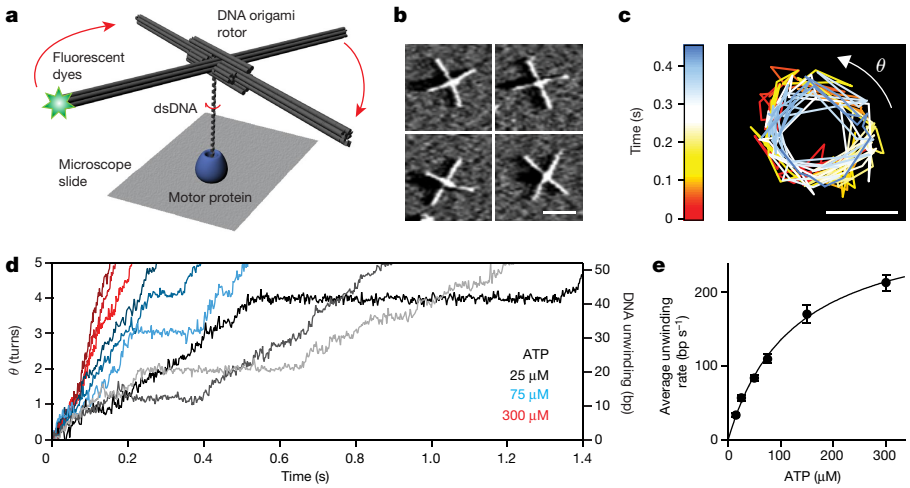


Fig. 1 | Single-molecule DNA rotation measurement using ORBIT. **a**, Schematic of the ORBIT method. The rotation of dsDNA relative to a surface-bound enzyme was amplified and detected using a DNA origami rotor labelled with fluorescent dyes. **b**, Atomic force microscopy images of DNA origami rotors. Representative images of more than ten independent biological replicates. Scale bar, 100 nm. **c**, Dye position trajectory from a rotor connected to dsDNA being unwound by RecBCD in the presence of 50 μM ATP. Colour indicates time. The rotation angle (θ) was measured using the dye position, imaged and tracked using a fluorescence microscope. Scale bar, 100 nm. **d**, Representative raw single-molecule DNA rotation trajectories showing processive unwinding by RecBCD at different concentrations of ATP (greyscale, 25 μM; blue hues, 75 μM; red hues, 300 μM). For display purposes, the initiation phase (discussed in Fig. 3) is not shown here, and traces are offset in angle and time such that processive unwinding starts at (0, 0). Data in **c** and **d** are representative examples from at least 3 independent biological replicates. **e**, ATP dependence of DNA unwinding rate by RecBCD. Data are mean ± s.e.m. (n = 29, 44, 76, 88, 52 and 86 (from left to right) trajectories, from at least 3 independent biological replicates at each condition). Solid line shows Michaelis–Menten fit (v_{max} = 304 ± 13 bp s^{-1}, K_M = 124 ± 12 μM). Data were recorded at 500 Hz (for 25–75 μM ATP) or 1 kHz (for 150–300 μM ATP), solution pH 8, 10% glycerol.

did not vary with the solution pH (Fig. 1e, Extended Data Fig. 4a) and is consistent with previously reported values[13–16]. Furthermore, we conducted stopped-flow experiments to measure the DNA unwinding rate in solution and obtained results that were comparable to the ORBIT measurements (Extended Data Fig. 5, Supplementary Table 4), which suggests that surface attachment did not substantially perturb the unwinding activity of RecBCD.

We observed three features during processive DNA unwinding in our single-molecule trajectories: unwinding, pausing and backtracking (Fig. 2a, b). RecBCD has previously been observed to pause and backtrack under an opposing force[16]. Our results showed that pausing and backtracking of RecBCD also occurred in the absence of a force; however, the pause durations and backtracking distances that we observed were substantially smaller than those observed under opposing forces[16]. The pause frequency decreased with increasing ATP concentration (Fig. 2c, Extended Data Fig. 4b), which suggests that pause entry preferentially occurs in the apo state. The average pause duration remained largely constant across all tested ATP concentrations (Fig. 2d, Extended Data Fig. 4c), which suggests that pause exit occurs through an ATP-independent process. Pauses were followed either by resumed unwinding or by backtracking. Backtracking distances were exponentially distributed with an average of around 6 base pairs, largely independently of ATP concentration (Fig. 2e, Extended Data Fig. 4d); these events were typically followed by a 'recovery pause' before DNA unwinding resumed. In contrast to the pauses during forward unwinding, the duration of the recovery pause depended on the concentration of ATP (Fig. 2f, Extended Data Fig. 4e), which suggests that these two different types of pause represent distinct enzymatic states (Extended Data Fig. 4f).

RecBCD processively unwinds dsDNA by using the motor subunits RecB and RecD to pull the two DNA strands across a pin-like structure in the enzyme[9]. However the active sites of these motors are situated several nanometres from the pin position[18], which suggests that an additional mechanism may be required for initial unwinding of dsDNA to bring the two strands to the active sites of the respective motors. Previous structural and biochemical studies have shown that RecBCD can unwind a few base pairs without ATP[18,19], which potentially provides such a mechanism, but direct evidence for the role of this activity during initiation is lacking. Notably, our ORBIT trajectories exhibited a distinct initiation phase between RecBCD binding and processive DNA unwinding (Fig. 3a, Supplementary Video 2). The initiation phase showed repetitive rotational transitions of the DNA between two well-defined states, with a step size of 169 ± 5° (n = 34 events) (Fig. 3a, Supplementary Video 2) that corresponds to about 5 base pairs of DNA unwinding. Processive unwinding consistently started from the higher-angle unwound state (green state in Fig. 3a). These transitions were observed to be quantitatively similar at two different concentrations of ATP (50 and 300 μM) and without ATP (Fig. 3b, c), which indicates that they were independent of ATP. Upon addition of ATP to complexes that were undergoing the transitions in the absence of ATP, the complexes initiated processive unwinding—again starting from the unwound state (Fig. 3b). Our results suggest that the transient, ATP-independent unwound state is an obligatory intermediate during RecBCD initiation on blunt-end DNA. Because the terminal base pairs of dsDNA in solution are frequently open[20], the wound state could either be fully base-paired or contain 1 or 2 unpaired bases. In either case, the single-stranded DNA (ssDNA) length in the unwound state (about 5–7 nucleotides (nt)) is comparable to that required to engage the RecB motor (about 6 nt, as inferred from the crystal structure of RecBCD[18]).

In addition to blunt-end DNA, natural substrates for RecBCD include dsDNA with either 3′ or 5′ ssDNA overhangs[9]. How RecBCD initiates on this diverse range of substrates remains unclear. We hypothesized that the transient, ATP-independent unwinding transitions observed on blunt-end dsDNA may not be required for initiation on substrates with ssDNA overhangs that are long enough to reach the corresponding motor domains. To test this hypothesis, we first designed a substrate with a 6-nt 3′ overhang, which should be long enough to engage the RecB motor[18]. We observed DNA unwinding mediated by RecBCD on this substrate, but not two-state transitions during the initiation phase (Fig. 3d, left, e, Extended Data Fig. 6), which is consistent with our hypothesis that contact of the RecB motor by an ssDNA overhang enables the enzyme to bypass the initial ATP-independent unwinding. We next tested whether contact of a 5′ ssDNA overhang with the RecD motor could have the same effect. We designed substrates without

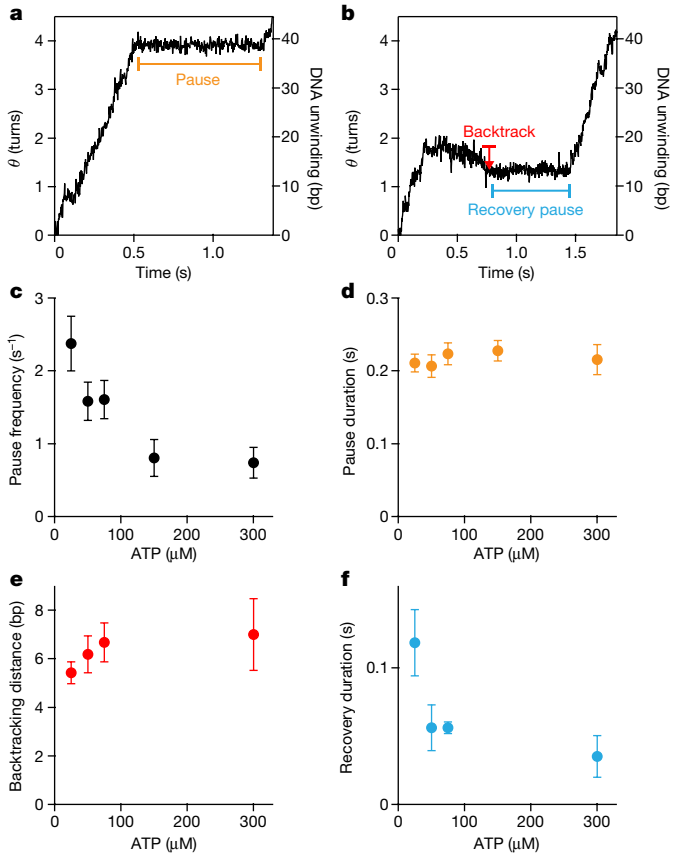


Fig. 2 | Pausing and backtracking during DNA unwinding induced by RecBCD. a, **b**, Single-molecule ORBIT trajectories of processive DNA unwinding by RecBCD at 25 μM ATP, showing examples of pausing and backtracking. Representative of 3 independent biological replicates. **c**, ATP dependence of the pause frequency per molecule. $n = 44$, 76, 88, 52 and 86 trajectories, from left to right. **d**, ATP dependence of the duration of pauses during forward unwinding. $n = 59$, 57, 84, 23 and 23 pauses, from left to right. **e**, ATP dependence of the backtracking distance. **f**, ATP dependence of the duration of recovery pauses that occur immediately after a backtracking event. In **e**, **f**, $n = 31$, 15, 25 and 13 events, from left to right. Data are shown as mean ± s.e.m. in **c**, **e**, or median ± s.d. of median from resampling in **d**, **f**. In **f**, 25 μM ATP data were statistically significantly different from 50, 75 and 300 μM ATP data; *P* values 0.03, 0.003 and 0.008, respectively; two-sided Kolmogorov–Smirnov test. Data were recorded at 500 Hz (for 25–75 μM ATP) or 1 kHz (for 150–300 μM ATP), solution pH 8, 10% glycerol.

3′ overhangs but with 10-nt or 15-nt 5′ overhangs, both of which should be long enough to engage RecD[18,21]. In contrast to substrates with 3′ overhangs, substrates with 5′ overhangs exhibited two-state transitions with a magnitude that matched the magnitude of the transitions observed with blunt-end dsDNA (Fig. 3d, right, f). Similar to the blunt-end substrate, the processive unwinding of the substrates with 5′ overhangs started after about 5 base pairs were unwound. The substrates with 5′ overhangs had a longer initiation phase (owing to a much longer dwell time in the wound state), but spent less total time in the unwound state before processive unwinding started (Fig. 3e, Extended Data Fig. 6). A similar dependence on the overhang geometry was observed in experiments conducted at both 50 μM and 300 μM ATP (compare Fig. 3, Extended Data Fig. 6 with Extended Data Fig. 7). The slower transition to the unwound state with substrates with 5′ overhangs may be due to a higher activation barrier, created by the additional contacts between the 5′ overhang and RecBCD[18]. Because initiation on the substrates with 5′ overhangs was strongly rate-limited by unwinding of the first approximately 5 base pairs, we hypothesized that initiation could be accelerated by weakening these base pairs. Indeed, conversion of the G-C pairs in the initial 5 base pairs to A-T reduced the average

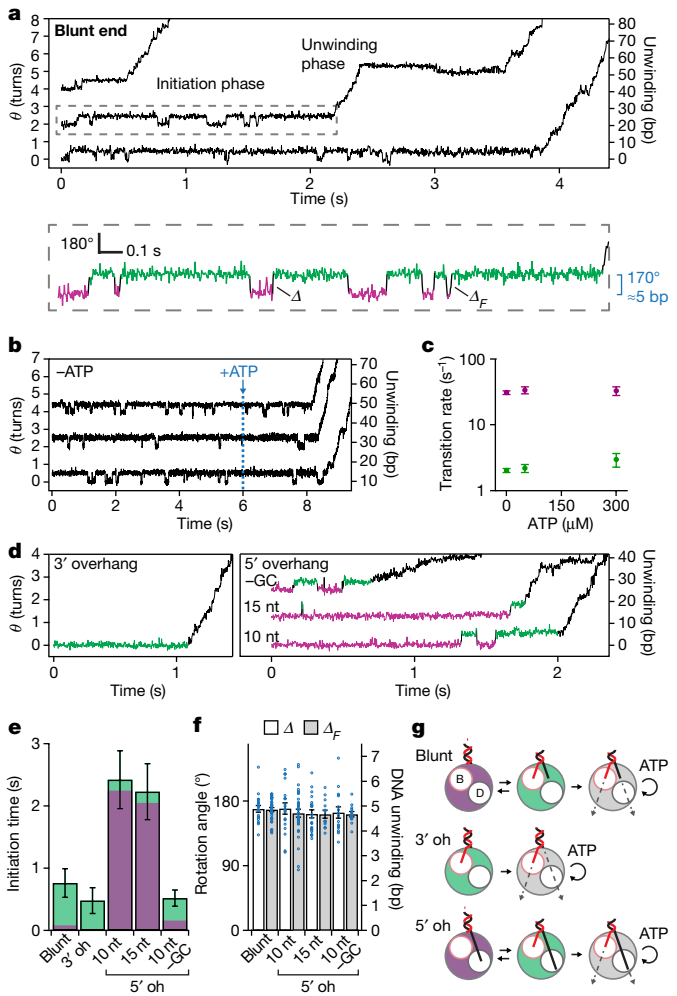


Fig. 3 | Initiation of RecBCD helicase activity at dsDNA breaks. **a**, Single-molecule trajectories showing initiation of DNA unwinding by RecBCD on blunt-end dsDNA. Initiation phase in the dashed box is magnified below, showing reversible transitions between wound (magenta) and unwound (green) states. Δ and Δ_F indicate step sizes of the reversible transitions and the final step before processive unwinding, respectively. **b**, RecBCD-induced unwinding transitions in the absence of ATP followed by addition of 50 μM ATP. Here, data recording started after RecBCD binding. **c**, Unwinding (magenta) and rewinding (green) transition rates show no ATP dependence. Unwinding rates are calculated from mean dwell times; error bars show propagated s.e.m. ($n = 409$, 293 and 97 (from left to right) events). Rewinding rates are calculated from mean dwell times considering kinetic competition; error bars show propagated s.e.m. (details and sample sizes are described in Supplementary Methods). **d**, Single-molecule trajectories showing the initiation of unwinding on dsDNA with a 6-nt 3′ overhang (left) or various 5′ overhangs (5′ oh; right). –GC denotes a 10-nt 5′ overhang without G-C in the initial 5 base pairs. **e**, Durations of initiation phase on the different substrates. Green and magenta portions indicate cumulative dwell times in magenta and green states, respectively. Mean ± s.e.m. *P* values (two-sided *t*-test): 0.36 for blunt-end versus 3′ overhang (3′ oh); 0.002 for blunt-end versus 10-nt 5′ overhang, 0.005 for blunt-end versus 15-nt 5′ overhang; and 0.0002 for 10-nt 5′ overhang versus 5′ overhang without G-C ($n = 104$, 90, 51, 46 and 137 (from left to right) trajectories from at least 3 independent biological replicates each). See Extended Data Fig. 6a for dot-plot overlay. **f**, Transition step sizes (Δ and Δ_F) for blunt-end and 5′ overhang substrates. Mean ± s.e.m. ($n = 34$, 18, 19, 33, 20, 13, 15 and 13 (from left to right) transitions, from at least 3 independent biological replicates each). **g**, Model for RecBCD initiation on dsDNA with different double-stranded break geometries. B and D indicate RecB and RecD motors, respectively. Trajectories in **a**, **b** and **d** are offset vertically for clarity and are representative of at least 3 independent biological replicates. Data were acquired at 50 μM ATP (**a**, **b**, **d**–**f**), 10% glycerol, solution pH 8, 500 Hz.

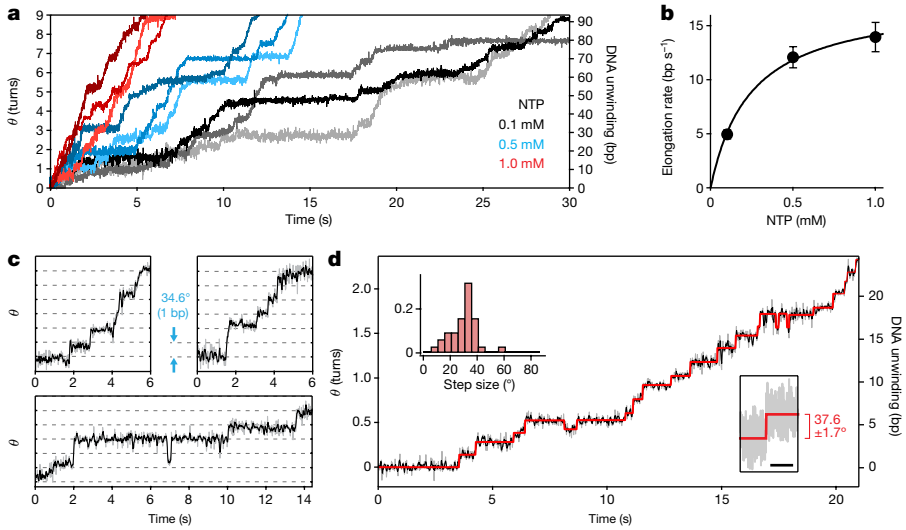


Fig. 4 | DNA rotation and rotational steps of a single base pair during transcription by RNAP, detected by ORBIT. a, Single-molecule trajectories of RNAP-driven DNA rotation at three concentrations of NTP (greyscale, 0.1 mM; blue hues, 0.5 mM; red hues, 1 mM) recorded at 200 Hz, solution pH 8. For clarity, the start of processive elongation is set as (0, 0). **b**, Dependence of elongation rate on NTP concentration at room temperature. The average rates were fit to Michaelis–Menten kinetics ($v_{max} = 17.5 \pm 0.8$ bp s^{-1}, $K_M = 240 \pm 30$ μM). Error bars indicate s.e.m. ($n = 32$, 31 and 39 (from left to right) trajectories from 3 independent biological replicates each). **c**, Example trajectories showing rotational steps at the scale of a single base pair, at low NTP concentration (grey, raw 50-Hz data; black, three-point boxcar filter). Horizontal dashed lines correspond to the average twist angle of a single base pair (34.6°). **d**, Example single-molecule trajectory of RNAP-driven DNA rotation (grey, raw 50-Hz data, black, three-point boxcar filter) and hidden Markov model fit (red). Top left inset, distribution of most probable step size that is >5° in each trajectory derived from hidden Markov model fits ($n = 31$ trajectories). Bottom right inset, high-resolution measurement of a RNAP-induced DNA rotation step recorded at 200 Hz (grey). Red lines represent means before and after the step. Scale bar is 1 s. Step size given as difference in mean ± s.e.m. for $n = 200$ data points on either side of the transition. Trajectories in **a**, **c** and **d** are representative of 3 independent biological replicates. Data in **c**, **d** were acquired with GTP, UTP, ATP and CTP concentrations at 5, 5, 2.5 and 1.25 μM, respectively, and solution pH 8.

initiation time of substrates with 5′ overhangs (Fig. 3e, Extended Data Fig. 6).

To further test our single-molecule results, we used an ensemble stopped-flow assay to measure the initiation kinetics of RecBCD (Extended Data Fig. 8a). We found that the addition of a 5′ overhang delayed unwinding, and that this delay was diminished by G-C to A-T conversion in the first 5 base pairs (Extended Data Fig. 8b, c), which corroborated our single-molecule results. In addition, we generated ensemble time-course predictions using the initiation and unwinding rates determined from single-molecule experiments, taking into account the fact that silicate glass coverslip surfaces are negatively charged (and thus lead to the local accumulation of H^+ ions and pH shift; Supplementary Discussion) and the fact that initiation rates for RecBCD were pH-dependent (compare Fig. 3e and Extended Data Fig. 9). The predicted time courses from single-molecule results quantitatively agreed with the stopped-flow measurements for all of the substrates that we tested, including blunt-end substrate and substrates with 3′ or 5′ overhangs, without any fitting parameters (Extended Data Fig. 8d–g).

Taken together, our results suggest that the engagement of the 3′ DNA strand with the RecB motor has an important role in the initiation of DNA unwinding, and that for DNA substrates that lack a 3′ overhang, an ATP-independent unwinding transition is used to engage the 3′ DNA strand with RecB (Fig. 3g). Processive, ATP-dependent DNA unwinding did not start immediately after the ATP-independent unwinding of the blunt-end substrate, or immediately after RecBCD binding to the substrate with a 3′ overhang sufficiently long to engage RecB. Additional waiting time was observed before processive unwinding in both cases, which indicates that another rate-limiting step is present. This additional waiting time was shorter for substrates with a 5′ overhang (Fig. 3e, Extended Data Fig. 6), which suggests a role for the 5′ overhang and RecD motor in initiation once the 3′ strand has reached RecB—consistent with previous suggestions of RecD involvement during initiation[21,22] and with a previous observation that the addition of a sufficiently long 5′ overhang to a DNA substrate that contains a 3′ overhang can accelerate initiation[21]. We also note that a RecBCD complex that contains an ATPase-deficient RecB mutant has previously been found to initiate processive unwinding on dsDNA with a 5′ overhang but not on a blunt-end dsDNA[23], which suggests that RecD can partially compensate for defective RecB in initiation.

To further demonstrate the general utility of our method, we used ORBIT to probe DNA rotation during transcription by RNAP. We generated stalled RNAP elongation complexes on dsDNA templates attached to origami rotors (by exclusion of one of the nucleoside triphosphates (NTPs)), adsorbed these complexes onto a coverslip and resumed elongation (by adding all four NTPs) while imaging. The ORBIT trajectories revealed that during transcription there was processive rotational motion punctuated by pauses (Fig. 4a), reminiscent of previously observed dynamics of the linear movements of RNAP[24–26]. The elongation rate measured by rotation exhibited a Michaelis–Menten dependence on NTP concentration ($K_M = 240 \pm 30$ μM, $v_{max} = 17.5 \pm 0.8$ bp s^{-1}) (Fig. 4b), which is consistent with previously reported values[6,24–26].

We next investigated the fundamental step-size of RNAP rotation during transcription. Optical tweezers studies have detected single-base-pair translocation steps of RNAP by measuring linear movements of RNAP during transcription under an applied force[27,28]. However, these single-base-pair steps have not been observed in the absence of an applied force. Furthermore, although RNAP generally rotates as it translocates along the DNA helix[6], rotational steps have not previously been observed. Our ORBIT trajectories recorded at low concentrations of NTP showed clear stepping patterns (Fig. 4c, d). In many segments of the trajectories, steps consistent with single-base-pair motion (about 35°) were visually apparent (Fig. 4c). Hidden Markov model analysis of the raw data revealed a preferred step size of approximately 35°, with most steps being distributed between 25° and 40° (Fig. 4d, Extended Data Fig. 10), consistent with the 27–40° range of the sequence-dependent twist angles between subsequent base pairs observed in the

structure of B-DNA[29]. Our results thus show that RNAP rotates in steps that correspond to translocations of single base pairs, which suggests a close coupling between the rotational motion of RNAP and the DNA helix at the scale of single bases.

To summarize, we have developed a method, ORBIT, for tracking single-molecule rotation with high resolution and throughput. By applying ORBIT to track DNA unwinding mediated by RecBCD, we have studied the distinct phases of initiation, unwinding, pausing and backtracking, and shed light on the mechanism of RecBCD initiation. When applied to the study of RNAP, ORBIT allowed us to observe rotational steps of single base pairs during transcription. Our studies demonstrate the power of DNA nanotechnology to amplify biomolecular movements for mechanistic studies. Considering that the rotation-tracking capabilities of our approach require only a standard fluorescence microscope and that the structural properties of the origami rotors can easily be customized, we anticipate that ORBIT will have broad applications in rotation measurements and the study of enzyme mechanisms. Combined with the ability to manipulate DNA origami with an external electric field[30], our approach could further enable a high-throughput platform for single-molecule force and torque spectroscopy. The coupling of origami structures to molecular machines that translocate on DNA could also enable the development of ATP-driven actuators for nanoscale applications.

Reporting summary

Further information on research design is available in the Nature Research Reporting Summary linked to this paper.

Data availability

The data that support the findings of this study are available from the corresponding author upon reasonable request.

Code availability

The single-molecule data were analysed using custom Python and Igor Pro code, available at https://github.com/altheimerb/python-sma/.

Online content

Any methods, additional references, Nature Research reporting summaries, source data, extended data, supplementary information, acknowledgements, peer review information; details of author contributions and competing interests are available at https://doi.org/10.1038/s41586-019-1397-7.

Received: 30 June 2018; Accepted: 17 June 2019;
Published online 17 July 2019.

1. Bryant, Z. et al. Structural transitions and elasticity from torque measurements on DNA. *Nature* **424**, 338–341 (2003).
2. Gore, J. et al. Mechanochemical analysis of DNA gyrase using rotor bead tracking. *Nature* **439**, 100–104 (2006).
3. Lebel, P., Basu, A., Oberstrass, F. C., Tretter, E. M. & Bryant, Z. Gold rotor bead tracking for high-speed measurements of DNA twist, torque and extension. *Nat. Methods* **11**, 456–462 (2014).
4. Deufel, C., Forth, S., Simmons, C. R., Dejgosha, S. & Wang, M. D. Nanofabricated quartz cylinders for angular trapping: DNA supercoiling torque detection. *Nat. Methods* **4**, 223–225 (2007).
5. Lipfert, J., van Oene, M. M., Lee, M., Pedaci, F. & Dekker, N. H. Torque spectroscopy for the study of rotary motion in biological systems. *Chem. Rev.* **115**, 1449–1474 (2015).
6. Harada, Y. et al. Direct observation of DNA rotation during transcription by *Escherichia coli* RNA polymerase. *Nature* **409**, 113–115 (2001).
7. Liu, S. et al. A viral packaging motor varies its DNA rotation and step size to preserve subunit coordination as the capsid fills. *Cell* **157**, 702–713 (2014).
8. Lipfert, J., Wiggin, M., Kerssemakers, J. W. J., Pedaci, F. & Dekker, N. H. Freely orbiting magnetic tweezers to directly monitor changes in the twist of nucleic acids. *Nat. Commun.* **2**, 439 (2011).
9. Dillingham, M. S. & Kowalczykowski, S. C. RecBCD enzyme and the repair of double-stranded DNA breaks. *Microbiol. Mol. Biol. Rev.* **72**, 642–671 (2008).
10. Rothemund, P. W. K. Folding DNA to create nanoscale shapes and patterns. *Nature* **440**, 297–302 (2006).
11. Douglas, S. M. et al. Self-assembly of DNA into nanoscale three-dimensional shapes. *Nature* **459**, 414–418 (2009).
12. Nomidis, S. K., Kriegel, F., Vanderlinden, W., Lipfert, J. & Carlon, E. Twist-bend coupling and the torsional response of double-stranded DNA. *Phys. Rev. Lett.* **118**, 217801 (2017).
13. Roman, L. J. & Kowalczykowski, S. C. Characterization of the helicase activity of the *Escherichia coli* RecBCD enzyme using a novel helicase assay. *Biochemistry* **28**, 2863–2873 (1989).
14. Bianco, P. R. et al. Processive translocation and DNA unwinding by individual RecBCD enzyme molecules. *Nature* **409**, 374–378 (2001).
15. Dohoney, K. M. & Gelles, J. Chi-sequence recognition and DNA translocation by single RecBCD helicase/nuclease molecules. *Nature* **409**, 370–374 (2001).
16. Perkins, T. T., Li, H.-W., Dalal, R. V., Gelles, J. & Block, S. M. Forward and reverse motion of single RecBCD molecules on DNA. *Biophys. J.* **86**, 1640–1648 (2004).
17. Liu, B., Baskin, R. J. & Kowalczykowski, S. C. DNA unwinding heterogeneity by RecBCD results from static molecules able to equilibrate. *Nature* **500**, 482–485 (2013).
18. Saikrishnan, K., Griffiths, S. P., Cook, N., Court, R. & Wigley, D. B. DNA binding to RecD: role of the 1B domain in SF1B helicase activity. *EMBO J.* **27**, 2222–2229 (2008).
19. Farah, J. A. & Smith, G. R. The RecBCD enzyme initiation complex for DNA unwinding: enzyme positioning and DNA opening. *J. Mol. Biol.* **272**, 699–715 (1997).
20. von Hippel, P. H., Johnson, N. P. & Marcus, A. H. Fifty years of DNA "breathing": reflections on old and new approaches. *Biopolymers* **99**, 923–954 (2013).
21. Wu, C. G. & Lohman, T. M. Influence of DNA end structure on the mechanism of initiation of DNA unwinding by the *Escherichia coli* RecBCD and RecBC helicases. *J. Mol. Biol.* **382**, 312–326 (2008).
22. Carter, A. R. et al. Sequence-dependent nanometer-scale conformational dynamics of individual RecBCD–DNA complexes. *Nucleic Acids Res.* **44**, 5849–5860 (2016).
23. Dillingham, M. S., Webb, M. R. & Kowalczykowski, S. C. Bipolar DNA translocation contributes to highly processive DNA unwinding by RecBCD enzyme. *J. Biol. Chem.* **280**, 37069–37077 (2005).
24. Forde, N. R., Izhaky, D., Woodcock, G. R., Wuite, G. J. L. & Bustamante, C. Using mechanical force to probe the mechanism of pausing and arrest during continuous elongation by *Escherichia coli* RNA polymerase. *Proc. Natl Acad. Sci. USA* **99**, 11682–11687 (2002).
25. Adelman, K. et al. Single molecule analysis of RNA polymerase elongation reveals uniform kinetic behavior. *Proc. Natl Acad. Sci. USA* **99**, 13538–13543 (2002).
26. Neuman, K. C., Abbondanzieri, E. A., Landick, R., Gelles, J. & Block, S. M. Ubiquitous transcriptional pausing is independent of RNA polymerase backtracking. *Cell* **115**, 437–447 (2003).
27. Abbondanzieri, E. A., Greenleaf, W. J., Shaevitz, J. W., Landick, R. & Block, S. M. Direct observation of base-pair stepping by RNA polymerase. *Nature* **438**, 460–465 (2005).
28. Righini, M. et al. Full molecular trajectories of RNA polymerase at single base-pair resolution. *Proc. Natl Acad. Sci. USA* **115**, 1286–1291 (2018).
29. Kabsch, W., Sander, C. & Trifonov, E. N. The ten helical twist angles of B-DNA. *Nucleic Acids Res.* **10**, 1097–1104 (1982).
30. Kopperger, E. et al. A self-assembled nanoscale robotic arm controlled by electric fields. *Science* **359**, 296–301 (2018).

Publisher's note: Springer Nature remains neutral with regard to jurisdictional claims in published maps and institutional affiliations.

© The Author(s), under exclusive licence to Springer Nature Limited 2019

Acknowledgements This work was supported in part by the National Institutes of Health. B.D.A. was supported by a National Institutes of Health Training Grant for the Graduate Program in Biophysics at Harvard University and a National Science Foundation Graduate Research Fellowship. M.D. was supported by a Howard Hughes Medical Institute International Student Research Fellowship. X.Z. is a Howard Hughes Medical Institute Investigator.

Author contributions P.K., B.D.A. and X.Z. conceived of the project and designed experiments. P.K. and B.D.A. performed ORBIT experiments and analysed the data. M.D., P.K. and P.Y. designed the origami structures. B.D.A., M.D. and P.K. prepared the origami structures. P.K. and M.D. performed atomic force microscopy and transmission electron microscopy imaging. P.K., B.D.A. and X.Z. wrote the manuscript with input from M.D. and P.Y.

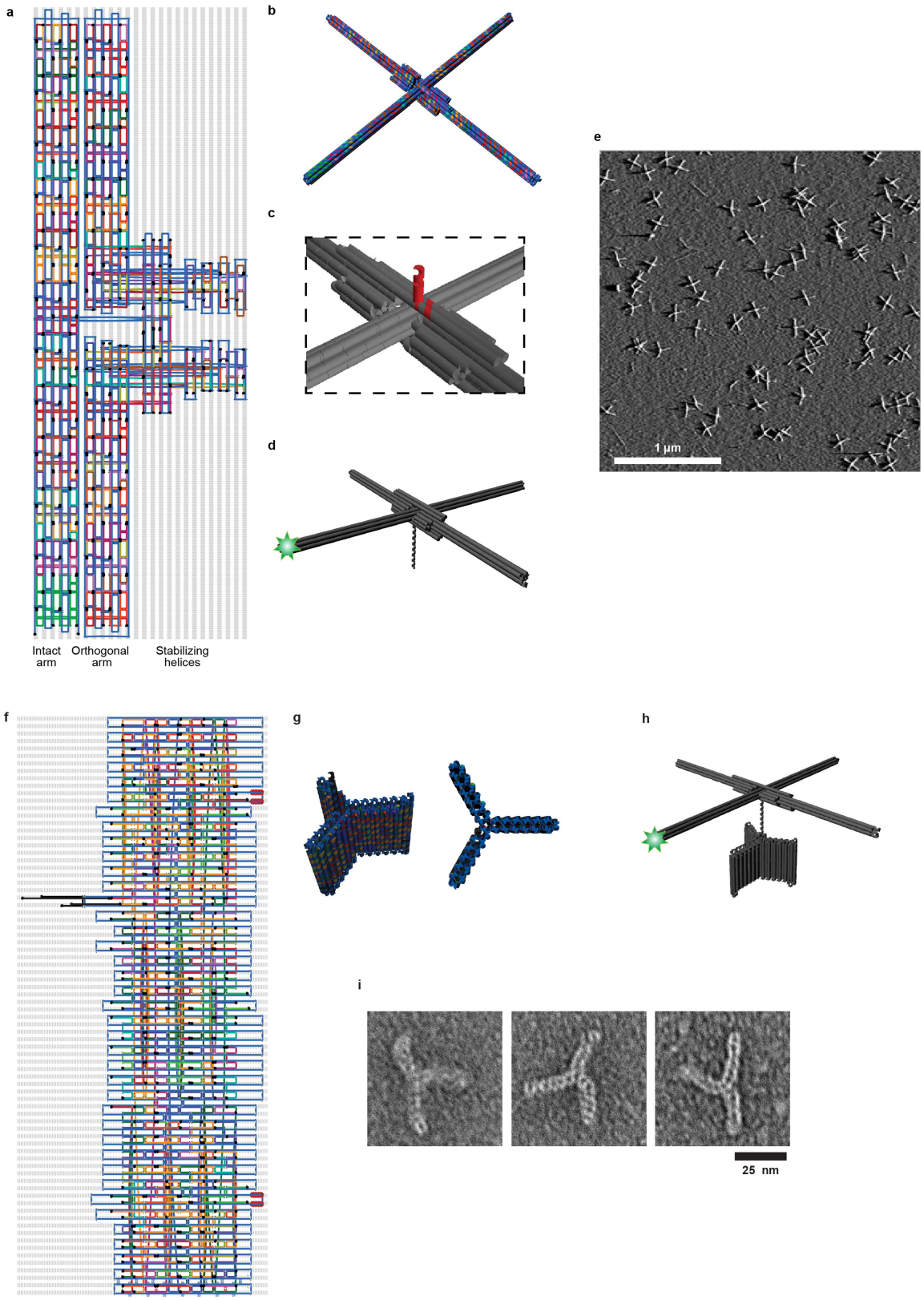
Competing interests The authors declare no competing interests.

Additional information

Supplementary information is available for this paper at https://doi.org/10.1038/s41586-019-1397-7.

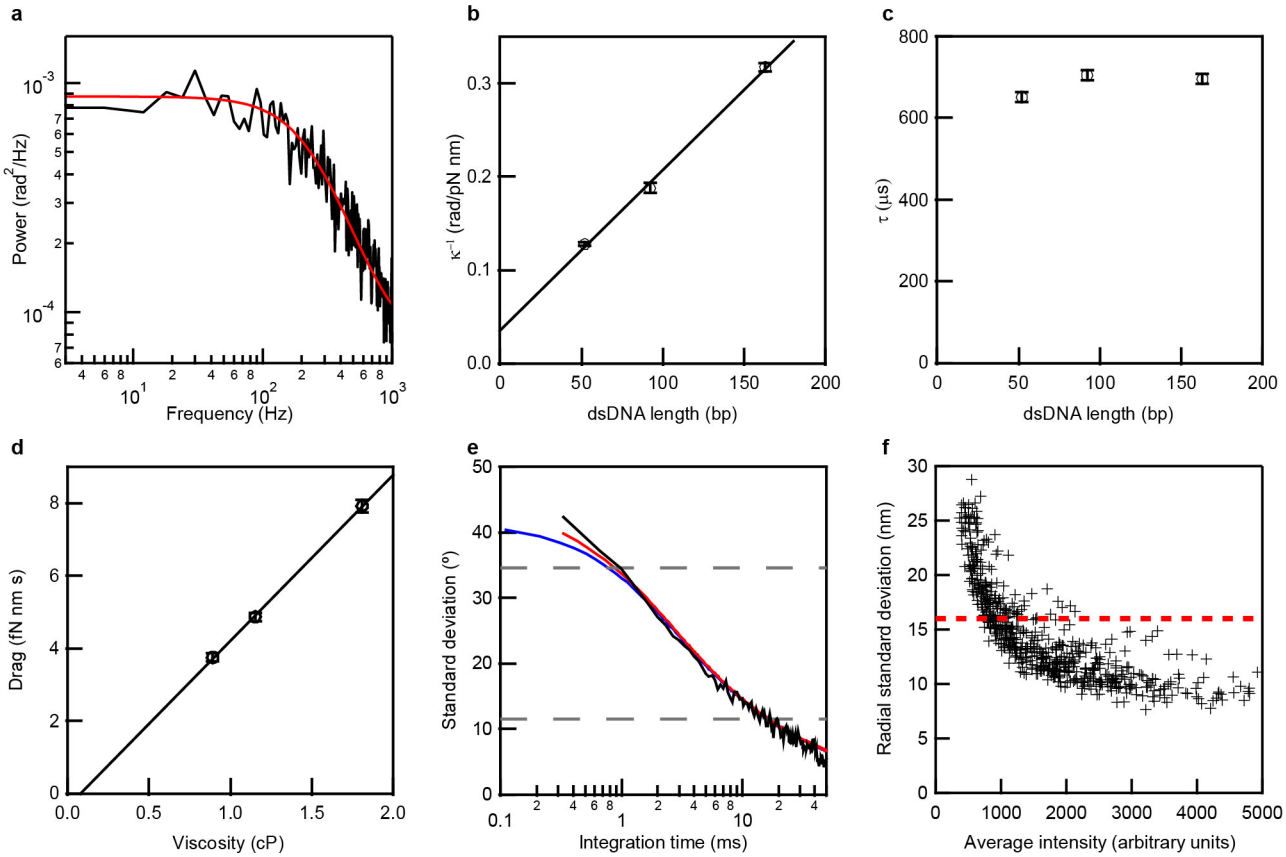
Correspondence and requests for materials should be addressed to X.Z.

Reprints and permissions information is available at http://www.nature.com/reprints.

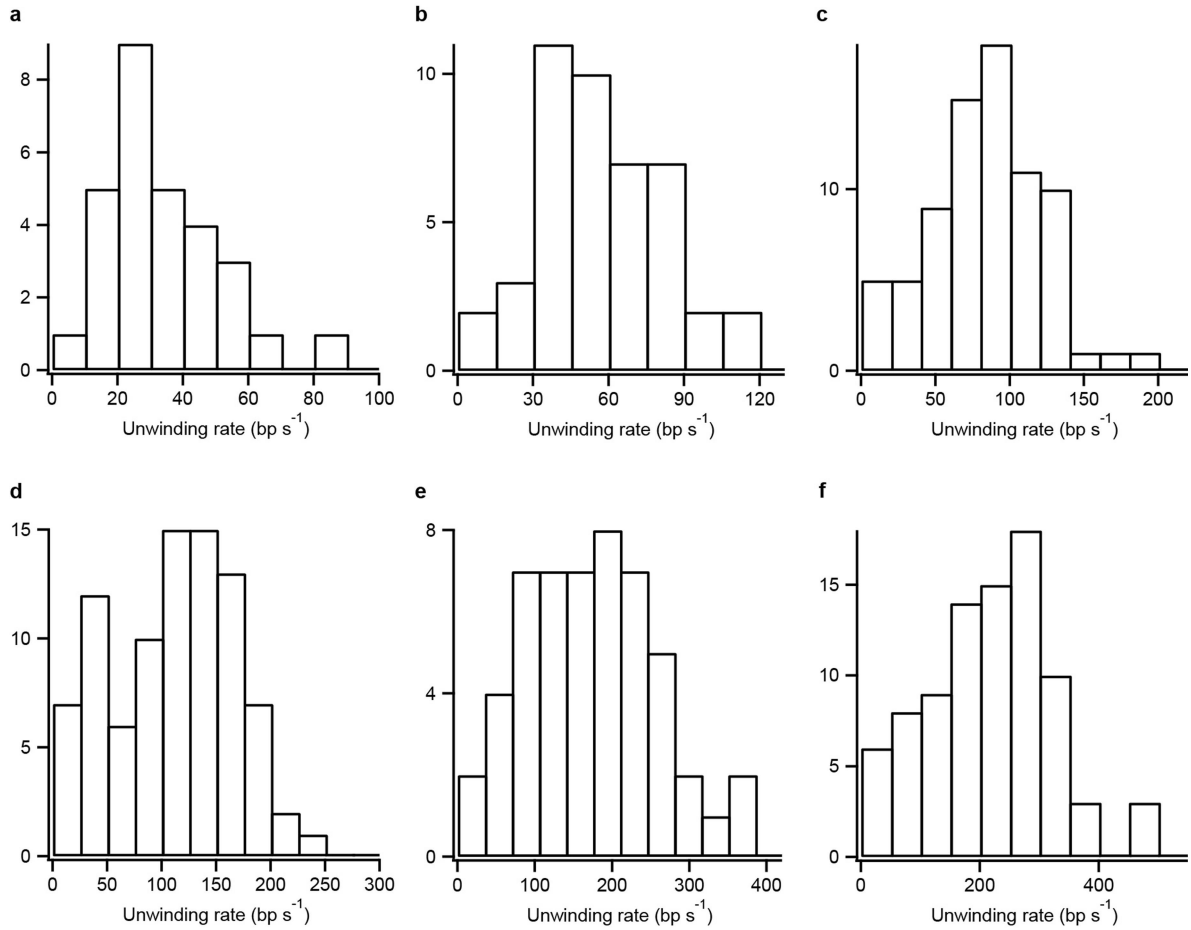


Extended Data Fig. 1 | See next page for caption.

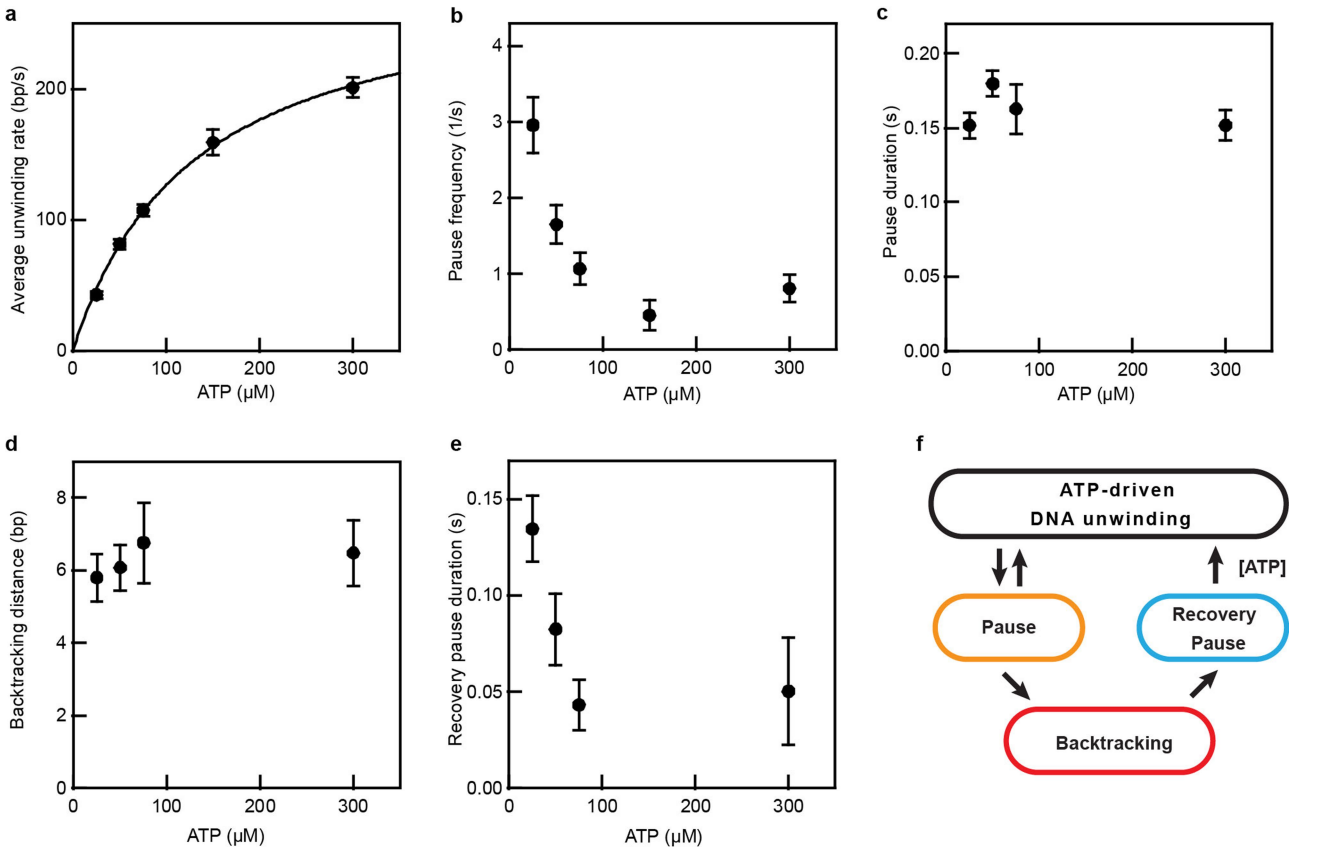
Extended Data Fig. 1 | Origami rotor and anchor designs. **a**, Routeing diagram of the origami rotor consisting of two 160-nm arms (Supplementary Table 1). The intact arm (a six-helix bundle) passes through a break in the orthogonal arm (two half-length six-helix bundles). Additional helices stabilize the junction. Two of these helices contain staple strands (black) that are extended from the centre of rotor (extension not shown; see **c**). Six staples within 14 nm of the end of the intact arm (light green) are labelled with Cy3 at their 3′ ends. **b**, Three-dimensional rendering of the rotor design. **c**, Magnified view showing the two staple strands (red) extending from the centre of the rotor, forming a 14-bp dsDNA segment and a 12-nt ssDNA overhang for ligation. **d**, The overhang is ligated to a longer piece of dsDNA, which serves as the substrate for the DNA-interacting enzyme. **e**, An atomic force microscopy image with large field of view of the origami rotors. Representative of more than ten independent biological replicates. Scale bar, 1 μm. **f**, Routeing diagram of the origami anchor consisting of three 20-nm wings, each made of a short 6-helix bundle motif (Supplementary Table 2). Several staple strands were extended with binding sites for biotin-labelled secondary oligomers for surface attachment. From the centre of the structure, three strands (black) were used to make an adaptor to allow ligation to additional DNA. Following the final strand crossover, the adaptor consists of 26 bp of dsDNA followed by a 12-nt ssDNA overhang. **g**, Three-dimensional renderings of the origami anchor. **h**, Origami structure used for characterizing the Brownian dynamics. The origami rotor, anchor and a dsDNA segment (as needed) were ligated together. The origami anchor is attached to the microscope surface using multiple biotin tags. **i**, Representative images of the origami anchors from one transmission electron microscopy experiment.



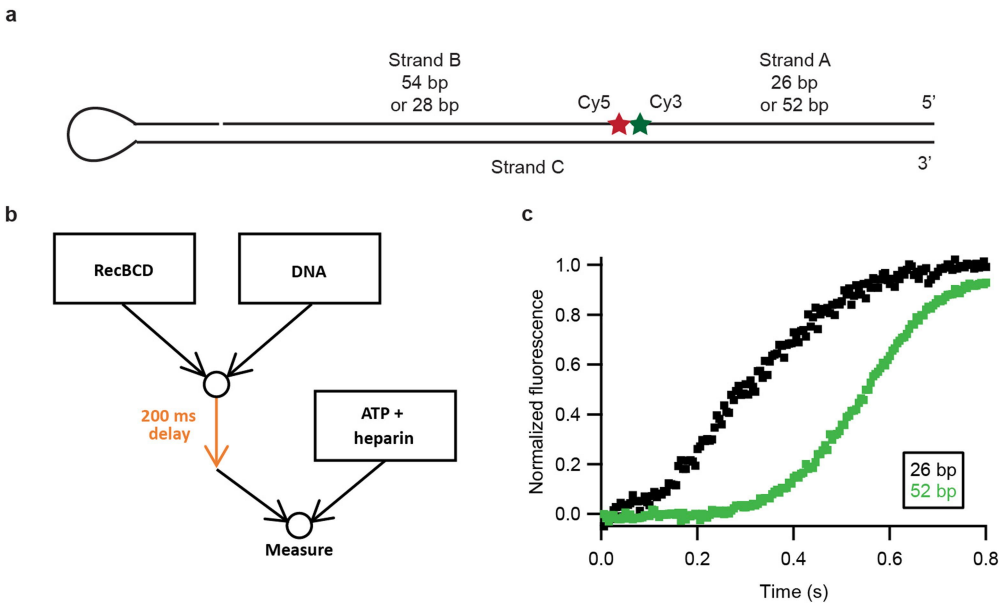
Extended Data Fig. 2 | Characterization of the angular and radial-position uncertainty of the origami rotor. a, Power spectrum showing the Brownian fluctuation in the angular position of the rotor attached to the anchor by 52 bp of dsDNA. Representative of 3 independent biological replicates. Red line shows the modified Lorentzian fit, as described in Supplementary Discussion, Supplementary Equation (1). This fit yields the torsional stiffness (κ) and hydrodynamic drag (γ). **b**, Dependence of the inverse of κ on the length of dsDNA segment between the rotor and origami. The slope of the linear fit yields the torsional stiffness per unit length of the dsDNA in the absence of an applied force (Supplementary Discussion, Supplementary Equation (3)), $C = 200 \pm 10$ pN nm^2 rad^{-1}, which is consistent with previous measurements under zero force[12]. The inverse of the y-offset from this fit, $\kappa_{other} = 30 \pm 8$ pN nm rad^{-1} (Supplementary Discussion, Supplementary Equation (3)), represents the torsional stiffness of the remainder of the structure, which is the equivalent of about 20 bp of dsDNA. **c**, Dependence of the relaxation time, $\tau = \gamma/\kappa$, on the length of the dsDNA segment between the rotor and anchor calculated using κ and γ derived from the power spectrum fit (Supplementary Discussion, Supplementary Equation (1)). Data in **b**, **c** are mean ± s.e.m. ($n = 203$, 195 and 133 (from left to right) rotor–anchor complexes from 3 independent biological replicates). **d**, Dependence of γ of the origami rotor on the viscosity of the buffer. The origami rotor was connected by a 92-bp dsDNA segment to the anchor. The different viscosities were achieved using 0%, 10% and 25% glycerol. Data are mean ± s.e.m. ($n = 195$, 210 and 150 (from left to right) rotor–anchor complexes from 3 independent biological replicates). **e**, Standard deviation of the angular positions of the rotor as a function of integration time. Black line shows the s.d. measured from a single rotor connected to the anchor with a 52-bp dsDNA segment tracked at 3 kHz after down-sampling to the indicated integration time. Representative of 3 independent biological replicates. Red and blue curves show predicted precision with and without (respectively) taking into account the contribution of localization uncertainty (Supplementary Discussion, Supplementary Equation (2)). $\kappa = 7.8$ pN nm rad^{-1}, $\gamma = 5.0$ fN nm s and localization uncertainty per frame $\sigma_L^2 = 0.038$ rad^2. κ and γ were derived from the measurements of multiple ($n = 203$) rotors with 52-bp dsDNA segment connecting the rotor to the anchor. σ_L^2 was estimated using the measurement uncertainty in radial position, and converted to an angular value using the radius of the circular trajectory. The crossing points of the top and bottom dashed lines with the s.d. versus integration time curve give the integration times required for detection of single-base-pair rotation (34.6°) with a signal-to-noise ratio of 1 and 3, respectively. **f**, Radial localization uncertainty (s.d.) during processive unwinding by RecBCD as a function of the average fluorescence signal intensity (mean) from individual rotors. Representative of 3 independent biological replicates. We apply a localization uncertainty threshold of 16 nm (0.1 pixel), shown in red, to select only trajectories with relatively high localization precision. All measurements were performed with 0% glycerol, except for **d**.



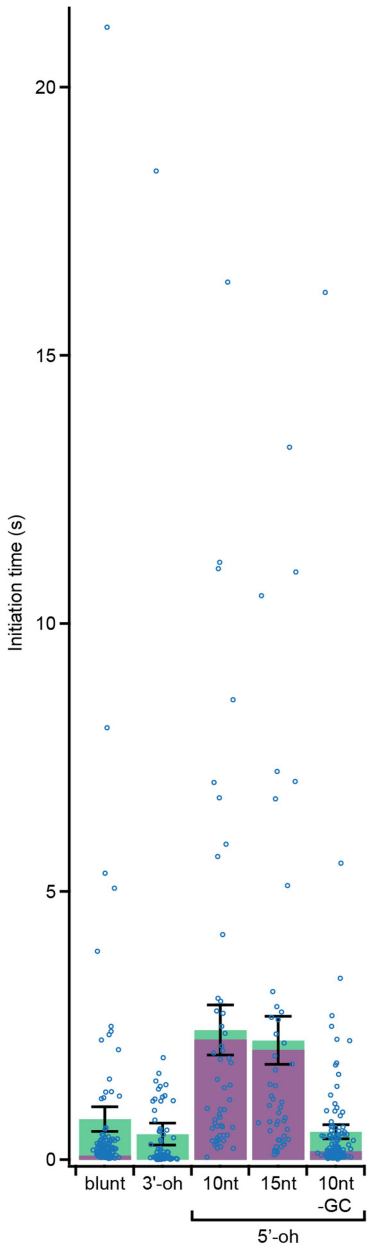
Extended Data Fig. 3 | Unwinding rate distributions. a–f, Histograms of the average unwinding rate of individual molecules at various concentrations of ATP concentrations (solution pH 8): 15 μM ATP (**a**), 25 μM ATP (**b**), 50 μM ATP (**c**), 75 μM ATP (**d**), 150 μM ATP (**e**) and 300 μM ATP (**f**).



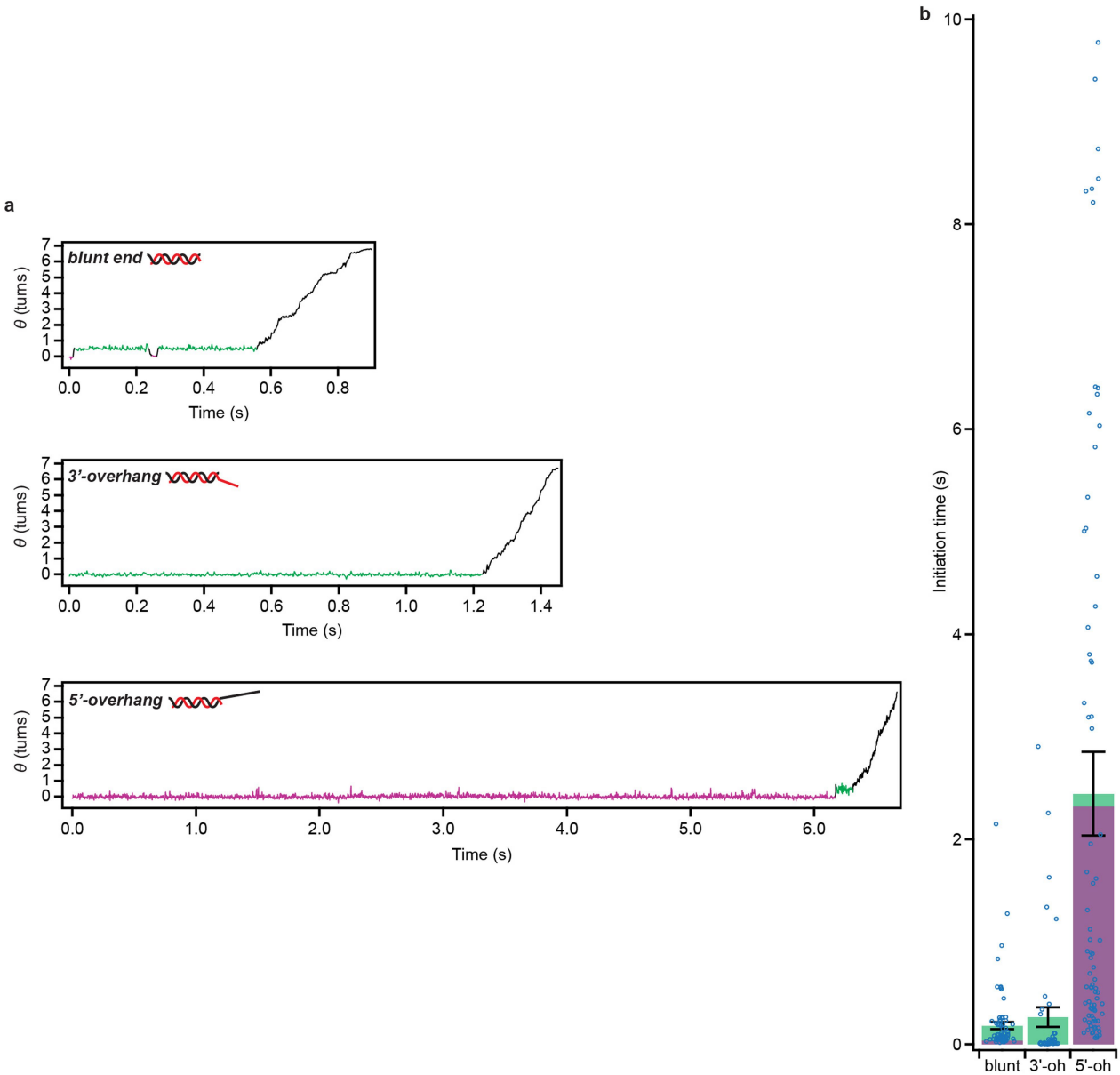
Extended Data Fig. 4 | RecBCD unwinding rate and pausing characteristics at solution pH 6. a, Average unwinding rate as a function of ATP concentrations fit to a Michaelis–Menten dependence with $v_{max} = 290 \pm 10$ bp s^{-1}, $K_M = 130 \pm 10$ μM. Data are mean ± s.e.m. ($n = 47$, 94, 80, 37 and 110 (from left to right) trajectories from at least 3 independent biological replicates for each condition). **b**, ATP concentration dependence of the pause frequency. Pause frequency was determined as the average number of pauses per second for each single-molecule trajectory. Data are mean ± s.e.m. ($n = 47$, 94, 80, 37 and 110 (from left to right) trajectories, from at least 3 independent biological replicates for each condition). **c**, Median duration of pauses during forward unwinding at various concentrations of ATP. The error bars are the s.d. of the median derived from resampling ($n = 76$, 62, 27 and 18 (from left to right) events, from at least 3 independent biological replicates for each condition). **d**, Mean backtracking distance at various concentrations of ATP. Data are mean ± s.e.m. ($n = 20$, 22, 16 and 10 (from left to right) events, from at least 3 independent biological replicates for each condition). **e**, Median recovery pause duration after a backtracking event at various concentrations of ATP. The error bars are the s.d. of the median derived from resampling. The *P* values for the differences between the 25-μM-ATP data point and the 50-, 75- and 300-μM-ATP data points are 0.05, 0.004 and 0.09, respectively, derived from two-sided Kolmogorov–Smirnov test of the distributions of the pause durations ($n = 20$, 22, 16 and 10 events for the 25, 50, 75, and 300 μM data points, respectively). Note that not all trajectories contain a backtracking event. Data were acquired at 10% glycerol, solution pH 6, 500 Hz. **f**, Schematic of a kinetic model of DNA unwinding induced by RecBCD. During DNA unwinding, pausing occurs frequently and some pauses lead to enzyme backtracking; the enzyme can exit the backtracking state and resume DNA unwinding through a recovery pause intermediate, which is distinct from the initial pause state.



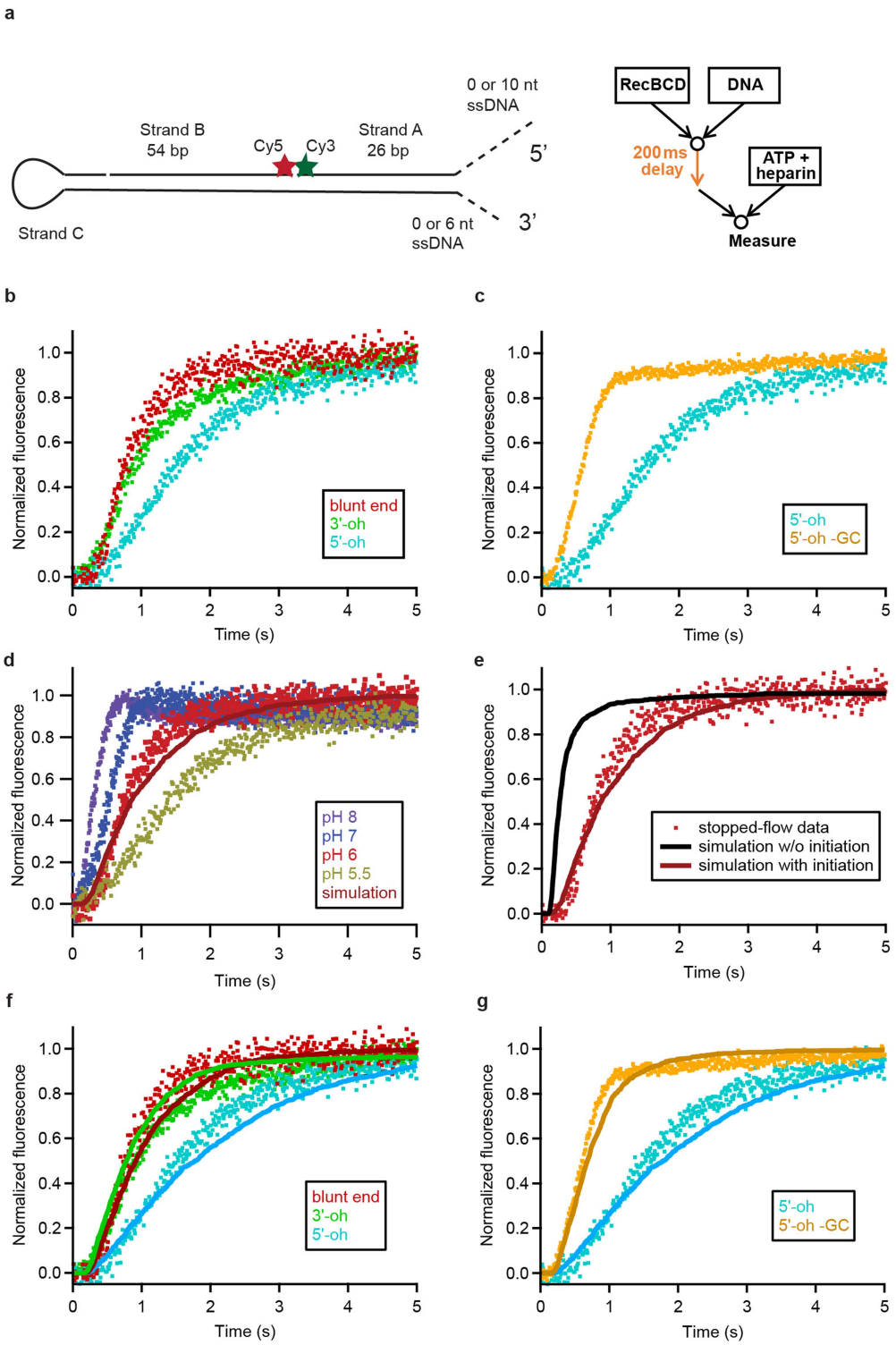
Extended Data Fig. 5 | RecBCD unwinding measured using ensemble stopped-flow assay. a, Design of the DNA substrate for the stopped-flow experiments[21]. The Cy3 on strand A is initially quenched by the Cy5 on strand B. RecBCD activity causes the dissociation of strand A, which results in an increase in fluorescence. The hairpin on the left side (strand C) ensures that activity can only begin from the right side. **b**, Dual-mixing stopped-flow experiment design. The RecBCD and DNA were mixed together for 200 ms in the delay loop before mixing with ATP and heparin, which prevents additional RecBCD–DNA binding after single turnover. **c**, Stopped-flow fluorescence measurements on blunt-end substrates with strand A having either 26 bp (black) or 52 bp (green), at 50 μM ATP and solution pH 8, 10% glycerol. Representative of at least 3 independent biological replicates. The ratio of the difference in strand A lengths for the two samples to the difference in measured half-rise times of the two samples allows the unwinding rate to be estimated as about 100 bp s^{-1}, assuming that the initiation kinetics are not different for these two substrates (because they have the same geometry and sequence at the double-stranded break). This unwinding rate is comparable to the 85 bp s^{-1} value determined by our single-molecule ORBIT measurements at the same concentrations of ATP.



Extended Data Fig. 6 | Distributions of durations of RecBCD initiation phase on various types of substrates at 50 μM ATP, solution pH 8. Reproduction of Fig. 3e, but with individual data points of the durations of initiation phase overlaid as dot plots. Bar graph statistics are described in Fig. 3e. Note that the distributions of the durations of the initiation phase are expected to be long-tailed exponential-like distributions, owing to the stochastic nature of kinetic transitions.

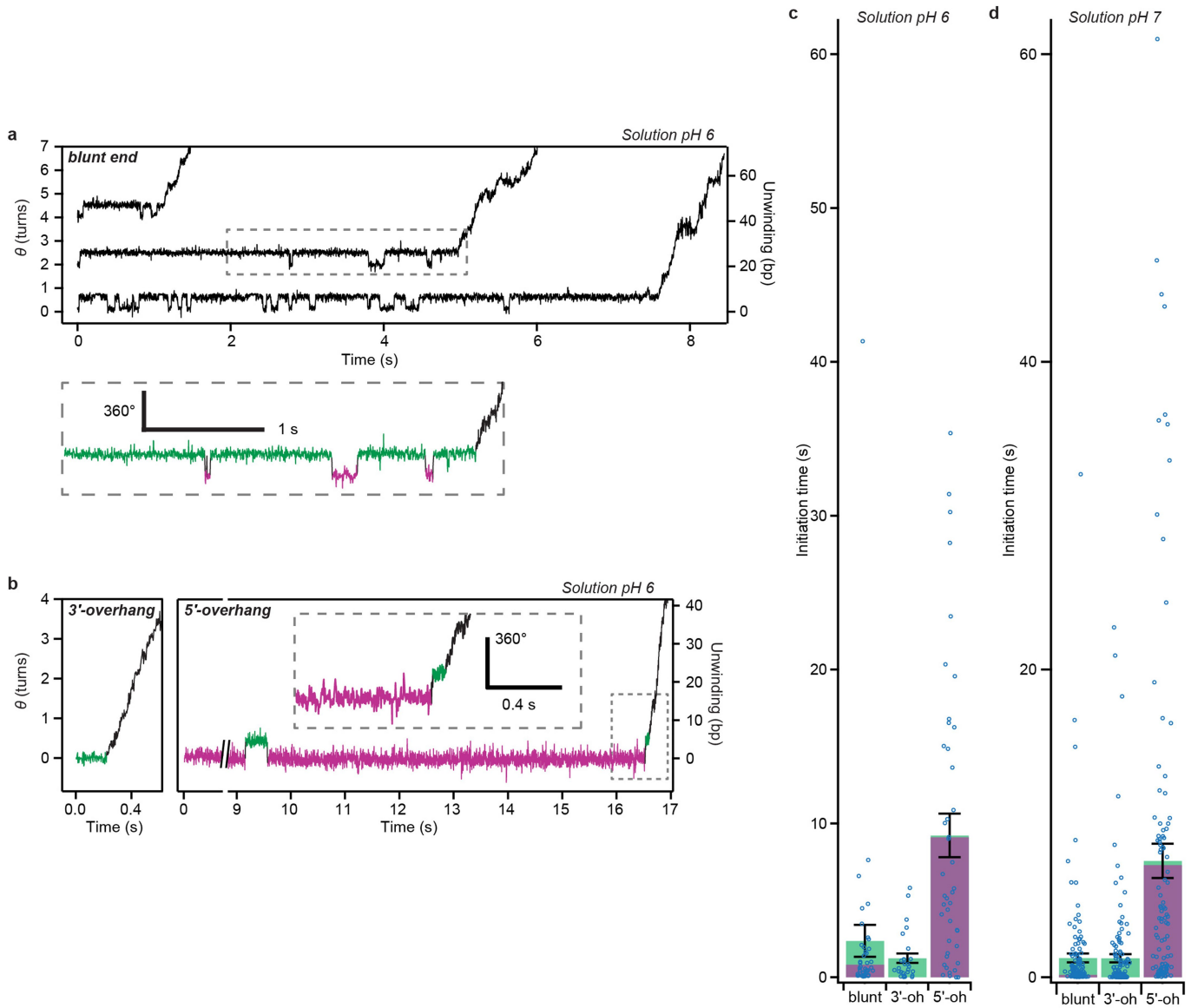


Extended Data Fig. 7 | RecBCD initiation kinetics at 300 μM ATP, solution pH 8. a, Example trajectories of initiation for the blunt-end DNA substrate and DNA substrates with 6-nt 3′ or 10-nt 5′ overhangs. Representative of at least 3 independent biological replicates. The green and magenta colour-coding is as described in Fig. 3a. **b**, Mean duration of initiation phase (total time from substrate binding until processive unwinding) for the blunt-end substrates and substrates with 6-nt 3′ or 10-nt 5′ overhangs. The green and magenta portions indicate the mean cumulative dwell times in the green and magenta states, respectively. Error bars are s.e.m. (n = 80, 44 and 85 (from left to right) trajectories from at least 3 independent biological replicates). Individual data points of the durations of initiation phase are overlaid as dot plots. Data were acquired at 300 μM ATP, solution pH 8, 10% glycerol, 500 Hz.

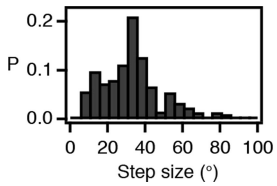


Extended Data Fig. 8 | See next page for caption.

Extended Data Fig. 8 | RecBCD unwinding kinetics measured using ensemble stopped-flow assay. a, Design of the DNA substrate for the stopped-flow experiments, as described in Extended Data Fig. 5a, b, except that either a 3′ or a 5′ ssDNA overhang was added as indicated (dashed lines), to prepare the respective substrates with overhangs. **b**, Stopped-flow fluorescence measurements for blunt-end substrates and substrates with 6-nt 3′ or 10-nt 5′ overhangs, showing slower kinetics for the substrate with the 5′ overhang. **c**, Stopped-flow fluorescence measurements for substrates with 10-nt 5′ overhang or 10-nt 5′ overhang with G-C pairs in the initial 5 base pairs converted to A-T. **d**, Comparison of predicted ensemble time course (red line) based on the initiation and unwinding rates derived from single-molecule data (collected at a solution pH 8) to measured stopped-flow time courses (coloured symbols) on the blunt-end substrate at several pH values. To simulate the ensemble time course without fit parameters, we modelled initiation as a single exponential process using our measured initiation rates from the single-molecule data, and unwinding as a series of 1-bp unwinding steps with each molecule in the simulation having an unwinding rate drawn from our experimentally measured distribution of unwinding rates from the single-molecule data. As expected, owing to the fact that the silica coverslip surface is charged (leading to local pH shift of about 2 units; see Supplementary Discussion), the predicted curve from the initiation and unwinding rates measured by single-molecule experiments at solution pH 8 (surface pH 6) matches the stopped-flow data measured at pH 6. **e**, Comparison of stopped-flow data (red symbols) for blunt-end substrates at pH 6 to the time courses predicted from both initiation and unwinding rates (red) or from unwinding rates alone (black line), derived from single-molecule data obtained at a solution pH 8 (surface pH 6). Thus, the inclusion of the initiation phase in the simulation is required to match the experimental results. **f**, **g**, Comparison of stopped-flow data at pH 6 (coloured symbols) shown in **b**, **c** to predicted ensemble time courses (lines with matched colour) using initiation and unwinding rates derived from the single-molecule data at a solution pH 8 (surface pH 6), as described for **d**. All stopped-flow experiments were conducted at 50 μM ATP, 10% glycerol, pH 6 (except for **d**, for which the pH is indicated in the legend) and are representative of at least 3 individual experiments for each condition. Plots with the same colours are duplicates of the same dataset placed in different panels for the purposes of comparison.



Extended Data Fig. 9 | RecBCD initiation kinetics at different pH values. a, Single-molecule trajectories showing RecBCD initiation on blunt-end substrates at 50 μM ATP, solution pH 6, 10% glycerol, recorded at 500 Hz. Arbitrary vertical offsets are applied to different trajectories for display purposes. The region in the dashed box is magnified below, in which the wound and unwound angle states are marked in magenta and green, respectively. **b**, Single-molecule substrates showing RecBCD initiation on substrates with 6-nt 3′ or 10-nt 5′ overhangs, under the same conditions. The region demarcated by the dashed box is magnified in the inset. Data in **a**, **b** are representative of at least 3 independent biological replicates. **c**, **d**, Mean duration of initiation phase (total time from substrate binding until processive unwinding) for the blunt-end substrate and substrates with 3′ or 5′ overhangs at solution pH 6 (**c**) and solution pH 7 (**d**), 50 μM ATP, 10% glycerol. The green and magenta portions indicate the cumulative dwell times in the green and magenta states, respectively. Error bars are s.e.m. ($n = 40$, 27 and 44 (from left to right) trajectories in **c**; $n = 149$, 154 and 108 (from left to right) trajectories in **d**, from at least 3 independent biological replicates for each condition). Individual data points of the durations of initiation phase are overlaid as dot plots.



Extended Data Fig. 10 | Additional analysis of RNAP base-pair stepping. Full probability distribution of forward step sizes (>5°) from the hidden Markov model analysis of the single-molecule trajectories of RNAP-induced DNA rotation. Here, all detected step probabilities in individual single-molecule trajectories are used to construct the histogram (instead of using the most-probable step size of each trajectory, as shown in the inset of Fig. 4d).

nature research

Corresponding author(s): Xiaowei Zhuang

Last updated by author(s): Jun 8, 2019

Reporting Summary

Nature Research wishes to improve the reproducibility of the work that we publish. This form provides structure for consistency and transparency in reporting. For further information on Nature Research policies, see Authors & Referees and the Editorial Policy Checklist.

Statistics

For all statistical analyses, confirm that the following items are present in the figure legend, table legend, main text, or Methods section.

n/a	Confirmed	
☐	☒	The exact sample size (*n*) for each experimental group/condition, given as a discrete number and unit of measurement
☐	☒	A statement on whether measurements were taken from distinct samples or whether the same sample was measured repeatedly
☐	☒	The statistical test(s) used AND whether they are one- or two-sided *Only common tests should be described solely by name; describe more complex techniques in the Methods section.*
☒	☐	A description of all covariates tested
☐	☒	A description of any assumptions or corrections, such as tests of normality and adjustment for multiple comparisons
☐	☒	A full description of the statistical parameters including central tendency (e.g. means) or other basic estimates (e.g. regression coefficient) AND variation (e.g. standard deviation) or associated estimates of uncertainty (e.g. confidence intervals)
☐	☒	For null hypothesis testing, the test statistic (e.g. *F*, *t*, *r*) with confidence intervals, effect sizes, degrees of freedom and *P* value noted *Give P values as exact values whenever suitable.*
☒	☐	For Bayesian analysis, information on the choice of priors and Markov chain Monte Carlo settings
☒	☐	For hierarchical and complex designs, identification of the appropriate level for tests and full reporting of outcomes
☒	☐	Estimates of effect sizes (e.g. Cohen's *d*, Pearson's *r*), indicating how they were calculated

Our web collection on statistics for biologists contains articles on many of the points above.

Software and code

Policy information about availability of computer code

Data collection	Single-molecule data was collected using custom Python code to control the microscope. This code is available at https://github.com/ZhuangLab.
Data analysis	The single-molecule data was analyzed using custom Python and Igor Pro code. This code is available at https://github.com/altheimerb/python-sma/

For manuscripts utilizing custom algorithms or software that are central to the research but not yet described in published literature, software must be made available to editors/reviewers. We strongly encourage code deposition in a community repository (e.g. GitHub). See the Nature Research guidelines for submitting code & software for further information.

Data

Policy information about availability of data

All manuscripts must include a data availability statement. This statement should provide the following information, where applicable:

- Accession codes, unique identifiers, or web links for publicly available datasets
- A list of figures that have associated raw data
- A description of any restrictions on data availability

The data that support the findings of this study are available from the corresponding author upon reasonable request and this data availability statement is included in the manuscript.

Field-specific reporting

Please select the one below that is the best fit for your research. If you are not sure, read the appropriate sections before making your selection.

☒ Life sciences ☐ Behavioural & social sciences ☐ Ecological, evolutionary & environmental sciences

For a reference copy of the document with all sections, see nature.com/documents/nr-reporting-summary-flat.pdf

Life sciences study design

All studies must disclose on these points even when the disclosure is negative.

Sample size	Sample sizes were not predetermined based on statistical methods, but were chosen according to the standards of the field (at least three independent biological replicates for each condition), which generated a sufficient number of single-molecule trajectories and gave sufficient statistics for the effect sizes of interest.
Data exclusions	We did not exclude any data from consideration. All single-molecule trajectories were included in the basic analysis; single-molecule trajectories showing processive DNA unwinding motion and high precision localizations were included for further enzyme-induced DNA rotation analysis, as detailed in Supplementary Methods, "Single-molecule data analysis for RecBCD" section, according to standards in the field.
Replication	Reported results were consistently replicated across multiple experiments with all replicates generating similar results.
Randomization	No randomization was necessary for this study because investigators were comparing designed DNA samples under well controlled conditions (e.g. variable ATP). No human or animal subjects were used in the study. Randomization is not generally used in this field.
Blinding	Investigators were not blinded. Blinding during collection was not needed because conditions were well controlled. Blinding during analysis was not feasible as the differences between samples under different conditions were visually apparent in the trajectories. Blinding is also not necessary because the results are quantitative and did not require subjective judgment or interpretation. Blinding is not typically used in the field.

Reporting for specific materials, systems and methods

We require information from authors about some types of materials, experimental systems and methods used in many studies. Here, indicate whether each material, system or method listed is relevant to your study. If you are not sure if a list item applies to your research, read the appropriate section before selecting a response.

Materials & experimental systems

n/a	Involved in the study
☒	☐ Antibodies
☒	☐ Eukaryotic cell lines
☒	☐ Palaeontology
☒	☐ Animals and other organisms
☒	☐ Human research participants
☒	☐ Clinical data

Methods

n/a	Involved in the study
☒	☐ ChIP-seq
☒	☐ Flow cytometry
☒	☐ MRI-based neuroimaging